A quantitative description of sea ice inclusions

Donald K. Perovich and Anthony J. Gow

U.S. Army Cold Regions Research and Engineering Laboratory, Hanover, New Hampshire

Abstract. Structurally, sea ice consists of an ice matrix with inclusions of brine and air. A quantitative description of the size of these inclusions is critical for both interpreting and modeling the electromagnetic properties of sea ice. Photomicrographs of ice thin sections were analyzed using a personal computer–based image-processing system to determine the number of inclusions, the inclusion size distributions, and statistics for brine pockets in young ice and first-year ice and for air bubbles in a multiyear hummock. Inclusions ranging in size from thousandths of square millimeters to a few square millimeters were measured. In all cases a two-parameter lognormal distribution fits the cumulative inclusion size distributions well (correlation coefficient greater than 0.99). This includes brine pockets in both granular and columnar ice and a range of brine volumes from 2% to 40%. As ice warms, and its brine volume increases, the size distribution shifts toward larger brine pockets. This increase in brine pocket size is particularly pronounced for brine volumes greater than 10% as individual brine pockets coalesce. Air bubbles are much larger than brine pockets, with mean major axis lengths of the order of millimeters for air bubbles and tenths of a millimeter for brine pockets. Observations of inclusion shape factors indicate that, in general, brine pockets are more elongated than air bubbles.

Introduction

Sea ice has an intricate and highly variable internal structure consisting of ice crystals and inclusions of brine and air. Because of the presence of brine, the ice microstructure is sensitive to changes in temperature and undergoes large changes on a seasonal basis. These changes in the physical state of the ice as well as its structure directly impact other properties of the ice, such as the electromagnetic and mechanical properties. The ability to formulate a detailed description of the physical state of sea ice is of fundamental importance to a wide range of geophysical problems and consequently has received considerable attention [*Weeks and Ackley*, 1982; *Eicken and Lange*, 1989; *Tucker et al.*, 1991; *Richter-Menge and Perovich*, 1992; *Jeffries et al.*, 1995]. Such descriptions can be used both to interpret other properties of the ice, such as the extinction coefficient, albedo, radar backscatter, and microwave emissivity, and to gain insight into ice processes, such as ice formation, decay, and deformation. Typically, descriptions include vertical profiles of ice temperature, salinity, brine volume, air volume, and density plus ice crystal structure [*Tucker et al.*, 1987].

As sea ice studies have become more sophisticated, the need for more detailed physical descriptions of sea ice microstructure has increased. For example, observations of the electromagnetic properties of sea ice indicate that there is considerable variability in such basic properties as the albedo [*Grenfell and Maykut*, 1977; *Grenfell and Perovich*, 1984; *Perovich*, 1990, 1994], the emissivity [*Eppler et al.*, 1992; *Grenfell et al.*, 1992], and the radar backscatter [*Onstott*, 1992] and that these properties depend on the physical state and structure of the ice. While much of the observed variability in electromagnetic properties can be explained in terms of basic physical properties such as brine volume and ice surface conditions [*Tucker et al.*, 1991, 1992], a more detailed characterization is needed.

For example, studies have indicated [*Perovich and Grenfell*, 1981; *Perovich*, 1996] that the optical properties of sea ice depend not only on the amount of brine but also on how the brine is distributed. This is not surprising in that we would expect that the scattering from 100 small inclusions would be different from the scattering from one large inclusion of equivalent volume. Thus a detailed physical description of sea ice microstructure is necessary to interpret and explain the observed variability in the electromagnetic properties of sea ice. Similarly, as electromagnetic models have advanced and become physically, rather than phenomenologically, based, the need for a more detailed description of the ice physical properties has increased [*Winebrenner et al.*, 1989, 1992].

The combined observational and theoretical need of the electromagnetic community has led to work that augments standard descriptions of sea ice with statistical characterizations of ice microstructure. *Arcone et al.* [1986] analyzed changes in the size and shape of brine inclusions coincident with warming of saline ice to interpret changes in the dielectric properties of the ice. *Lin et al.* [1988] continued this analysis to describe the microscale variability of the microwave permittivity of young sea ice in terms of a correlation function. Such a description is an important element in microwave models using strong fluctuation theory [*Tsang and Kong*, 1981; *Stogryn*, 1984; *Vallese and Kong*, 1981; *Lin et al.*, 1988].

The advent of powerful and inexpensive personal computer–based image-processing equipment has greatly enhanced the ability to statistically characterize ice microstructure [*Perovich and Hirai*, 1988; *Eicken*, 1993]. *Perovich and Gow* [1991] used such image-processing techniques to describe sea ice microstructure in terms of the mean and standard deviation of the permittivity plus the correlation function. *Eicken* [1993] developed image-processing techniques to quantify ice textural parameters such as grain size and pores in the ice. The size and shape of air bubbles found in hummocks and ice under melt ponds were examined by *Shokr and Sinha* [1994]. Grain sizes in

first-year sea ice have been investigated by *Johnston and Sinha* [1995].

The focus of this paper is to investigate the inclusion size distribution for sea ice. The motivation of this work is to quantitatively describe elements of ice microstructure that can relate the observed variability in electromagnetic properties of sea ice to changes in the physical state of the ice and to provide the detailed physical description of the ice needed for electromagnetic models. The scattering of electromagnetic radiation in sea ice is determined in large part by the number, size, and shape of sea ice inclusions: the brine pockets and the air bubbles. A quantitative description of the air bubbles and brine pockets is essential to understanding scattering in the ice and therefore is a critical input parameter for sea ice radiative transfer models at both optical and microwave wavelengths [*Grenfell*, 1983, 1991; *Winebrenner et al.*, 1989, 1992].

In this paper, brine pockets will be characterized during the growth and evolution of first-year ice. New ice and young ice [*Armstrong et al.*, 1973] grown under quiescent and turbulent conditions and thick first-year ice will be examined. The characteristics of air bubbles found in a multiyear hummock will also be described. In addition, the influence of ice temperature on brine pocket size distribution will be investigated. For these cases we will present a description of the relevant physical properties, basic statistics regarding the inclusions (e.g., number, range, median area, mean area), and the inclusion size distribution. We will place this statistical ice characterization in the context of the standard ice physical properties and show how the inclusions are influenced by such parameters as ice temperature and growth conditions.

Experimental Methods

This work was done as part of a large interdisciplinary effort directed toward understanding relationships between the physical, optical, and microwave properties of sea ice and linking observations with theory. To interpret and to model the electromagnetic observations, a detailed description of the physical state and structure of the ice was needed. This description included vertical profiles of ice temperature, salinity, density, brine volume, air volume, and crystallography determined from analysis of ice cores [*Tucker et al.*, 1987]. Temperatures and salinities were measured using an Omega temperature probe and a Beckman solubridge and were accurate to ±0.1°C and ±0.2 parts per thousand (ppt), respectively. While this description was a necessary component of the ice characterization, it alone was not sufficient for the interpretation of the observations and the development of models; a statistical description of the ice microstructure was also needed.

A three-dimensional description of the volume of the inclusions would be ideal. However, this is not practical using current technology and a compromise to two dimensions must be made. The statistical description was obtained by analyzing photomicrographs of ice thin sections [*Perovich and Gow*, 1991, 1992]. Horizontal sections were used, since they provide a better representation of the brine pocket structure due to the vertical nature of the ice platelet structure and the brine incorporation characteristics. The thicknesses of the ice thin sections were selected to be large enough to contain the entire volume of individual inclusions but small enough so that the inclusions did not obscure one another. As a result the thin sections were about 1 mm thick, except for the multiyear hummock sections, which were approximately 3 mm thick due to the larger dimensions of the air bubbles. Since the brine inclusions tend to be vertically elongated and oriented, these 1-mm-thick sections represent the horizontal cross-sectional area of the inclusions. In the case of air bubbles, which are less elongated and are not vertically oriented, the 3-mm-thick sections provide the maximum cross-sectional area of the air bubble.

In order to highlight the air bubbles and brine pockets and to facilitate the image processing, the sections were photographed using plain transmitted light. A large format 125-mm by 175-mm bellows extension camera was used to photograph the samples. A 7× magnification was selected to be high enough to make the brine pockets and air bubbles visible and low enough to ensure that the area of the photograph contained many such inclusions.

Once the thin section photographs were obtained, they were analyzed on a personal computer using off-the-shelf software [*Optimas*, 1995] and customized software [*Perovich and Hirai*, 1988]. A scanner was used to digitize the images into a two-dimensional array of pixels. Each pixel was assigned a gray shade from 0 to 255, depending on the brightness of that small portion of the image. The scale of the scanned images was typically 25 mm by 18 mm, with the length of a single pixel being approximately 0.03 mm. Since an inclusion must contain at least a few pixels to be resolvable, at this magnification we can only distinguish inclusions larger than approximately 0.003 mm^2.

The first step in the image processing, partitioning the image into its constitutive components of ice, brine and air, is critical. This is done by exploiting differences in gray shade between ice and its inclusions. The basic assumption underlying the image processing is that the inclusions are the darkest features in an image. In general, this appears to be true; however, problems can arise with grain boundaries, which can be as dark as the inclusions, and the centers of air bubbles, which can be as light as the ice. Starting with a good image greatly facilitates the image processing procedure, so special care was taken preparing and photographing the thin sections to ensure that the inclusions were clearly distinguishable from the ice. Thin sections were made with a uniform thickness with no marks or blemishes on the top or bottom and then were photographed under uniform illumination. For the young ice and first-year ice samples analyzed, brine volumes were much greater than air volumes, and it was assumed that all the inclusions were brine pockets. In the case of the multiyear hummock, brine drainage had completely desalinated the ice and all the inclusions were air bubbles. Particular care was taken in analyzing the pancake ice thin sections where both air bubbles and brine pockets were present. In this case the air bubbles were selected manually.

The gray shade cutoff for the ice-brine partitioning was determined using the brine volume of the sample. The fractional area of the sample defined as brine was set equal to this brine volume. The brine volume of a sample was calculated by using independent measurements of sample temperature and salinity and the relationship of *Frankenstein and Garner* [1967]:

$$v_b = S\left(0.0532 - \frac{4.919}{T}\right),$$

where v_b is the brine volume (percent), S is the salinity (parts per thousand), and T is the temperature (degrees Celsius). The temperature and salinity measurements were made using samples from the same ice core from which the thin sections were prepared. There are uncertainties associated with this method

of partitioning the image into ice and brine. Since brine pockets are elongated ellipsoids rather than infinitely long cylinders, this approach tends to overestimate the brine volume. Complicating matters even further are small-scale changes in salinity, which can easily vary by a few parts per thousand over distances of a few centimeters. Because of these factors, there is approximately a 20% uncertainty in brine volume estimates and consequently in the ice-brine partitioning. For example, a reported brine volume of 10% lies between 8% and 12%. For the hummock ice, air bubbles were easier to identify and we were able to segment between air and ice visually.

After the images were partitioned, it was relatively straightforward, using standard off-the-shelf software [Optimas, 1995], to identify the inclusions and then analyze their characteristics. Our focus was on the number and size distribution of the inclusions, though we also investigated other parameters, including inclusion major axis length, shape factor, and orientation. After the number and size of the inclusions were determined, the next step was to formulate a general description of the inclusion size distribution. One option was to take the list of inclusion sizes and generate a histogram showing what fraction of the inclusions were in different size ranges. However, such a description is sensitive to the size ranges selected and is difficult to treat in a general sense. A better approach is to determine either the cumulative distribution function (CDF) or its derivative, the probability density function (PDF) of the inclusion sizes [Papoulis, 1965]. Using a sorted list of inclusion sizes, we were able to determine a observed cumulative distribution function for the inclusion sizes. In principle, the PDF can be determined by numerically differentiating the observed CDF; however, in practice, this procedure generated a PDF that was unacceptably noisy.

To further generalize the results and to be able to calculate a PDF, we decided to determine if the observed CDF could be represented by a function. We examined many different functions, using curve fitting software [Jandel Scientific, 1994], to determine the form of the inclusion size CDF. While the software can examine thousands of functions, we were considerably more selective. Our selection criteria for the best fit function were (1) a commonly used probability function, such as a power law, exponential, logarithmic, normal, or lognormal, not just a polynomial expansion, (2) a correlation coefficient close to 1, (3) a minimization of the number of free parameters, and (4) a satisfying of the CDF boundary conditions of equaling 0 for very small inclusions and 1 for very large inclusions. With these criteria in mind we analyzed the observed CDFs for over 40 thin sections encompassing a wide range of ice types and including cases with brine pockets and with air bubbles. Overall, the data were fit best by a cumulative lognormal distribution of the form

$$CDF(A) = \frac{1}{2} \, erfc \left[\frac{-(\ln A - \mu)}{\sigma \sqrt{2}} \right]$$

where A is the cross section area of the inclusion (square millimeters). This distribution does an excellent job of fitting the wide range of cases studied, with correlation coefficients typically greater than 0.99. And it does so using only two parameters, μ and σ, which are the mean and standard deviation of the variable ln (A), respectively. For a lognormal distribution, antilog(μ) is the median of the variable A. It must be remembered that the lognormal fit and the particular values of μ and σ are determined based on measurements of inclusions larger than 0.003 mm^2. We do not know if extending the

analysis to include smaller inclusions would change the values of the parameters or even the form of the function. The probability density function for this distribution is

$$PDF = \frac{dCDF}{dA} = \frac{1}{\sqrt{2\pi\sigma^2}} \frac{1}{A} \exp \left[\frac{-(\ln A - \mu)^2}{2\sigma^2} \right]$$

Lognormal distributions are common in nature and occur when random processes contribute multiplicatively to a variable, rather than additively as in a normal distribution [Sachs, 1978]. The lognormal distribution has effectively described sea ice features such as pressure ridge keels [Davis and Wadhams, 1995], grain coarsening in snow [Colbeck, 1987], as well as other naturally occurring processes in ocean biooptics [Campbell, 1995], geology, and biology [Sachs, 1978].

Results

We processed over 40 thin section photographs, examining microstructure of different ice types under a range of conditions. Ice grown in the field under natural conditions and ice grown in the laboratory under controlled conditions were studied. Examples of both granular ice and columnar ice were investigated. While the focus was on brine pockets, air bubbles in a multiyear hummock were also analyzed. In each of these cases, basic inclusion statistics were calculated, the inclusion size distribution was determined, and the best fit lognormal cumulative distribution was generated.

Young Ice

In the Arctic, much of the production of young ice occurs in leads. This young lead ice typically has high salinity and a large brine volume. Depending on growth conditions, its initial crystal structure can be either granular or columnar. Once a continuous ice sheet has formed on the sea surface, the underlying ocean is isolated from the cold air so latent heat is extracted through the ice sheet by thermal conduction. Further crystallization now occurs by direct freezing of seawater to the underside of the ice. Such freezing is called congelation growth and typically yields vertically elongated columnar crystals. Within this columnar ice zone a crystal substructure is developed consisting of pure plates of ice interspersed with parallel layers of brine inclusions. These inclusions represent the residual brine that cannot be rejected from the freezing interface and becomes segregated as inclusions between the pure ice plates. Each crystal of sea ice thus contains a number of plates, between which are sandwiched layers of brine pockets. The plate spacing (brine layer separation distance) can vary from a few tenths of a millimeter to more than a millimeter, depending mainly on the rate of freezing [Nakawo and Sinha, 1984]. Such a specialized freezing process also impacts the bulk salinity of the resultant ice, the more rapid the freezing the narrower the plate spacing and the saltier the ice and vice versa. With the onset and full development of congelation growth those crystals with their c axes parallel to the ice/water interface quickly begin to eliminate crystals with less-favored orientations. This planar distribution of c axes often transforms into one in which the c axes become aligned. Such alignment of the c axes is commonplace in shore-fast ice and can be correlated with the direction of persistent current motion at the ice/water interface [Weeks and Gow, 1978, 1980]. Such directional control of the current over the c axis orientation of sea ice also impacts significantly on the electromagnetic properties.
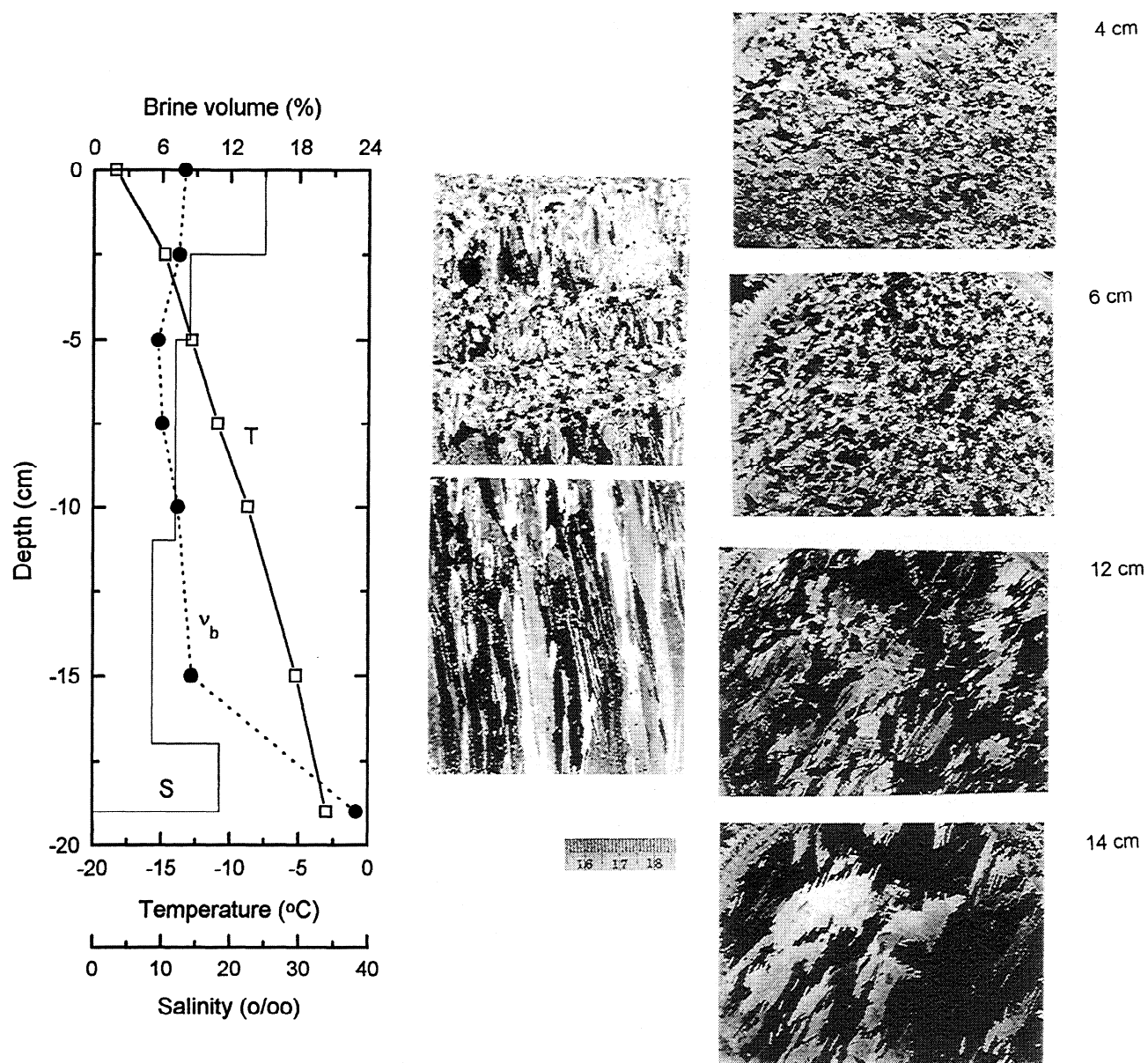
Figure 1. Physical properties of young ice grown in a springtime lead in the Beaufort Sea. Plotted are ice temperature (open squares), brine volume (solid circles), and salinity (bars). Ice structure is illustrated in a vertical thin section and four horizontal sections from depths of 3 cm, 6 cm, 12 cm, and 14 cm. The thin section photographs were taken between crossed polarizers.

The physical properties of young ice sampled during a field study of springtime leads [*LEADEX Group*, 1993] are summarized in Figure 1. The ice was 20 cm thick after 2.5 days of growth during April at air temperatures of $-25°C$ to $-30°C$. The ice was quite salty, with salinities from 10 to 20 ppt. As a result of snow blowing into the lead and frazil formation in the water, the top 6 cm of the ice was granular. Beneath this layer, congelation ice growth was dominant and the remainder of the ice consisted of columnar crystals elongated in the vertical with c axes in the horizontal. The horizontal section photographs (Figure 1) also illustrate how the grain size increased with depth.

Two horizontal thin sections (Figure 2) were selected from this lead ice at depths of 12 and 19 cm for inclusion size analysis. The brine volumes of the 12-cm and 19-cm sections were 7% and 23%, respectively. The larger brine volume for the 19-cm sample was a result of higher temperatures and salinities near the bottom of the ice. The photographs show columnar ice with vertically oriented platelets with c axes horizontal. The images were partitioned into ice and brine, and the brine pockets were identified using the techniques described earlier. There were more and larger brine pockets near the bottom of the ice, with the 19-cm section having roughly three brine pockets per square millimeter with a mean area of $0.060 \ mm^2$ and the 12-cm section 1.4 brine pockets per square millimeter with a mean area of $0.036 \ mm^2$ (Table 1).

The observed CDFs for these two photographs, along with the best fit CDF and PDF, are plotted in Figure 2. In general, there is excellent agreement between the observed and the fitted lognormal CDFs. There is some deviation for small inclusions, with the lognormal distribution estimating more inclusions than observed. However, this is consistent with the
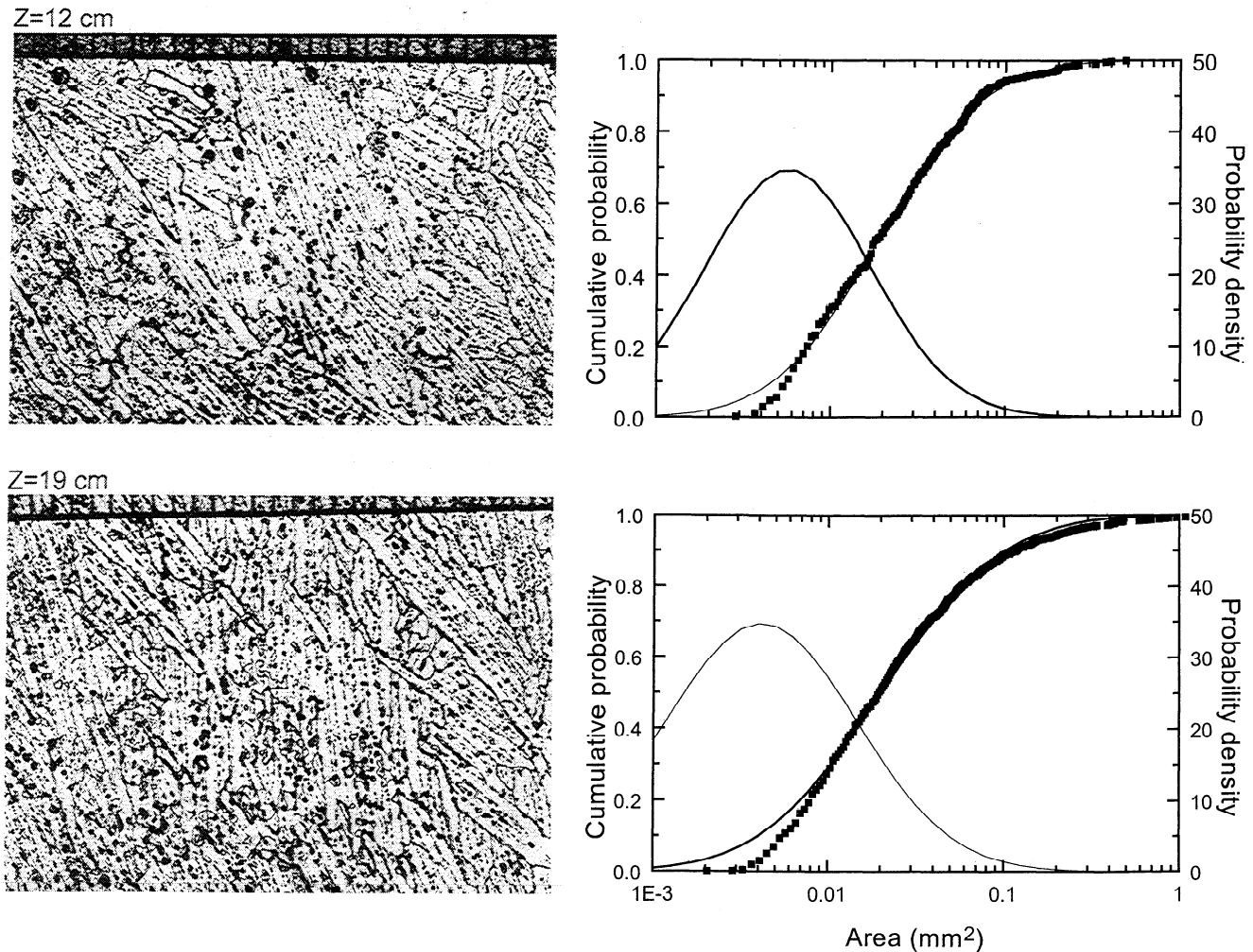
Figure 2. Horizontal thin sections of columnar young ice. Sections were from depths (Z) of 12 and 19 cm. Plotted are observed (solid squares) and the best fit cumulative brine pocket size distributions. Also plotted is the probability density function determined from the best fit cumulative distribution. Scale is provided by a ruler in the top of the photographs which has demarcations of 1 mm.

limitations of the image processing system, which has difficulty distinguishing very small inclusions and tends to underestimate their number.

For some applications the shape of the inclusions is also of interest. One common measure of shape is circularity, defined as $C = P^2/A$, where P is the inclusion perimeter and A the area. The smallest possible value of C is 4π, corresponding to a circle. As the shape deviates from a circle, C increases. Another similar, commonly used measure is the compactness [Shokr and Sinha, 1994], which is the inverse of the circularity. Circularities computed for the brine inclusion in the two sections in Figure 2 were large, with mean values of 30–35 and median values of 26–28. The median circularities correspond to elongated ellipses with a 4:1 major axis to minor axis ratio.

Pancake Ice

Pancake ice is another major young ice type. It is predominant in the Antarctic [Gow et al., 1987; Lange et al., 1988] and is commonly found in the marginal ice zones of the Arctic [Tucker et al., 1991]. Initial ice formation at or near the sea surface occurs in the form of small platelets and needle-like crystals called frazil. With continued freezing a soupy mixture

of sea water and unconsolidated frazil called grease ice is created. In the presence of a sustained wave field, pancake ice is usually formed. Pancakes range in size from tens of centimeters to more than 3 m in diameter and often display irregular raised rims due to constant bumping and squeezing up of frazil crystals around their edges. Once consolidated, pancake ice sheets continue to thicken downward by direct freezing of the seawater, generally in the form of columnar congelation ice [Weeks and Ackley, 1982].

As part of a laboratory study of young ice we used a wave maker (a motor-driven paddle) to grow pancake ice in an 8- × 20- × 2-m sea ice pond (Figure 3a). A wave field was maintained in the pond for the first 14 hours of growth, during which time a semiconsolidated sheet of frazil developed into pancake ice that was 12 cm thick. This growth occurred at an ambient air temperature of −15°C. After this initial period of pancake ice formation the wave maker was turned off and ice growth was continued under a refrigerated roof at a relatively high temperature of −5°C for 1 month. Because of the warmer air temperatures, ice growth rates were small and salinities were low. At the end of a month the ice thickness had increased to 30 cm and the ice had undergone some desalination

Table 1. Summary of Inclusion Statistics and Cumulative Size Distribution

	Physical Properties					Statistics			Area, mm²		Major Axis Length, mm		Perimeter, mm		Circularity		Cumulative Lognormal		
Z, cm	H, cm	T, °C	S, ‰	V_b, %	Type	Number	V, mm³	N	Mean	Median	Mean	Median	Mean	Median	Mean	Median	Antilog (μ)	σ	R^2
Beaufort Sea: Springtime Lead																			
6	15	−9.0	16.0	12.0	C	757	409	1.9	0.034	0.020	0.34	0.27	0.94	0.73	33.5	28.0	0.0195	1.03	0.998
12	20	−7.0	9.0	7.0	C	461	329	1.4	0.036	0.019	0.32	0.25	0.89	0.70	30.0	26.0	0.0191	1.10	0.997
19	20	−3.0	15.0	23.0	C	967	309	3.1	0.060	0.020	0.40	0.26	1.21	0.70	34.9	28.0	0.0202	1.26	0.995
Pancakes																			
1	32		Air		G	61	261	0.2	0.276	0.134	0.63	0.51	1.91	1.51	18.2	16.6	0.1271	1.24	0.995
1	32	−6.9	6.2	4.9	G	203	261	0.8	0.046	0.010	0.30	0.18	0.94	0.50	34.9	29.0	0.0105	1.06	0.987
10	32	−5.1	3.3	3.7	C	317	284	1.1	0.021	0.012	0.28	0.22	0.74	0.57	35.2	30.1	0.0120	1.07	0.997
20	32	−3.5	3.1	4.8	C	446	268	1.7	0.018	0.008	0.23	0.17	0.63	0.46	33.7	29.9	0.0081	0.91	0.995
30	32	−2.3	4.5	9.9	C	863	265	3.3	0.018	0.008	0.27	0.19	0.73	0.50	42.1	35.6	0.0084	1.06	0.993
First-Year Ice																			
4	172	−6.9	8.6	7.1	G	269	272	1.0	0.056	0.025	0.37	0.27	1.14	0.81	32.1	27.3	0.0240	1.27	0.998
10	172	−6.9	8.9	7.7	C	474	275	1.7	0.031	0.018	0.30	0.24	0.84	0.69	29.1	25.9	0.0177	1.09	0.999
30	172	−6.7	7.2	6.4	C	593	274	2.2	0.019	0.013	0.24	0.21	0.66	0.56	27.0	24.0	0.0132	0.85	0.999
75	172	−5.7	5.2	5.5	C	456	282	1.6	0.023	0.013	0.26	0.20	0.71	0.55	27.6	23.7	0.0130	1.01	0.996
119	172	−4.6	4.9	5.9	C	456	261	1.7	0.023	0.011	0.25	0.20	0.72	0.54	30.6	26.3	0.0114	1.05	0.995
171	172	−2.0	5.5	14.6	C	1236	275	4.5	0.020	0.010	0.26	0.20	0.77	0.57	37.3	33.0	0.0106	1.04	0.997
Multiyear Hummock																			
Total					D	1040	13,000	0.08	0.637	0.106	0.84	0.52	2.59	1.49	22.2	19.1	0.1126	2.01	0.996
hummock																			
2	>200	0.0	0.0	0.0	D	184	1115	0.165	0.610	0.064	0.80	1.18	2.43	0.42	22.3	19.3	0.0777	2.07	0.985
7	>200	0.0	0.0	0.0	D	62	976	0.064	0.825	0.123	0.83	1.46	2.78	0.55	21.5	17.8	0.0960	2.19	0.986
12	>200	0.0	0.0	0.0	D	42	862	0.049	0.929	0.199	1.17	2.06	3.85	0.73	25.5	20.5	0.2294	1.99	0.991
21	>200	0.0	0.0	0.0	D	87	1348	0.065	0.659	0.059	0.84	1.13	2.53	0.42	21.2	18.6	0.0865	2.19	0.973
24	>200	0.0	0.0	0.0	D	108	1425	0.076	0.540	0.057	0.74	1.03	2.27	0.36	22.5	18.9	0.0686	2.20	0.972
27	>200	0.0	0.0	0.0	D	101	1181	0.086	0.392	0.233	0.80	1.96	2.38	0.68	19.9	17.6	0.1751	1.66	0.988
32	>200	0.0	0.0	0.0	D	117	1253	0.093	0.888	0.066	0.73	1.17	2.12	0.40	19.7	18.3	0.0728	2.00	0.991
50	>200	0.0	0.3	~0	D	104	1387	0.075	0.616	0.074	0.87	1.36	2.79	0.49	25.6	21.7	0.0848	1.73	0.982
53	>200	0.0	0.3	~0	D	89	1116	0.080	0.457	0.261	0.88	2.33	2.85	0.76	23.0	20.4	0.2577	1.28	0.991
57	>200	0.0	0.3	~0	D	66	1048	0.063	1.151	0.230	1.30	2.62	3.99	0.82	23.9	20.0	0.2488	2.08	0.995
64	>200	0.0	0.3	~0	D	80	1182	0.068	0.253	0.110	0.64	1.47	1.88	0.54	21.2	18.9	0.1000	1.43	0.996
Warming Sequence																			
18	20	−20.0	8.2	2.6	C	209	174	1.2	0.015	0.008	0.19	0.15	0.52	0.41	24.3	21.8	0.0080	0.96	0.990
18	20	−10.0	8.2	4.3	C	291	174	1.7	0.016	0.008	0.21	0.16	0.57	0.42	27.0	23.5	0.0085	0.97	0.991
18	20	−5.0	8.2	8.4	C	607	174	3.5	0.016	0.008	0.20	0.16	0.57	0.43	27.7	24.2	0.0083	0.99	0.994
18	20	−2.0	8.2	20.6	C	1169	174	6.7	0.022	0.012	0.24	0.19	0.72	0.54	31.2	26.7	0.0117	1.09	0.998
18	20	−1.0	8.2	40.8	C	942	174	5.4	0.075	0.016	0.35	0.22	1.26	0.62	35.9	26.9	0.0165	1.39	0.998

Z is the depth within the ice; H is the ice thickness, T is the temperature; S is the salinity; V_b is the brine volume; Type is the ice type where C is columnar, G is granular and D is desalinated; V is the volume, N is the number density (inclusions per cubic millimeter); and R^2 is the regression coefficient.

A

B
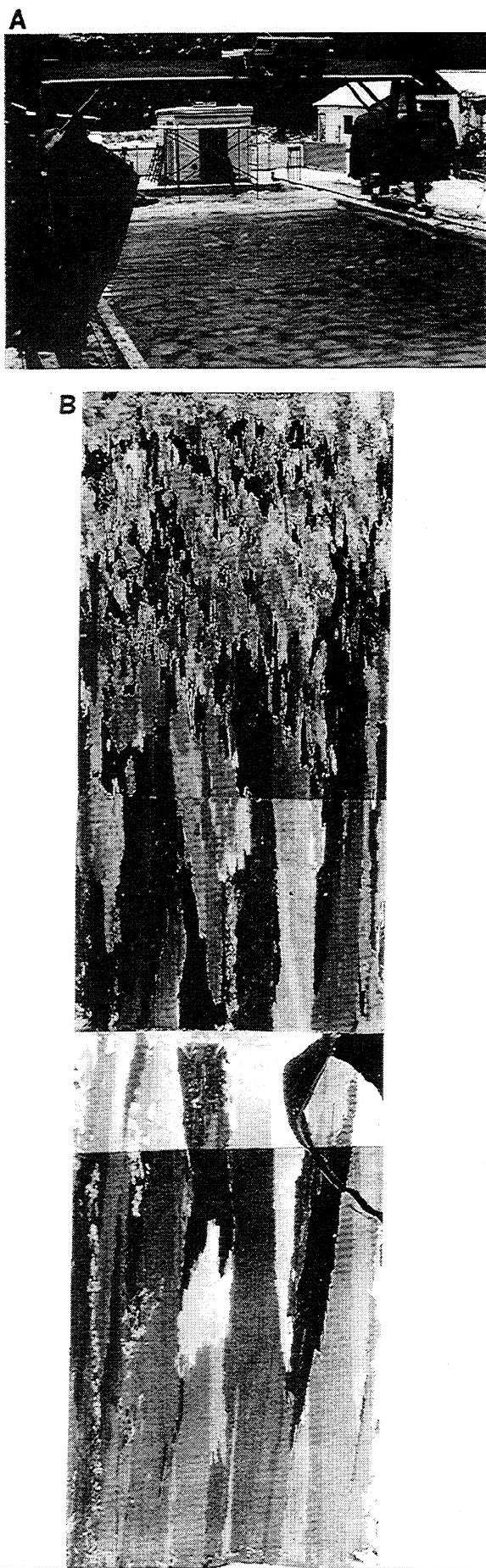
with salinities in the 3–6 ppt range and brine volumes between 4% and 10%. Without the agitation provided by the wave-maker, congelation ice growth dominated, and the bottom 18 cm of the ice had a columnar structure with c axes oriented in the horizontal. The abrupt shift from frazil to columnar ice is illustrated by the vertical thin section shown in Figure 3b.

Horizontal thin sections were selected for analysis from depths of 1, 10, 20, and 30 cm. Photographs of these thin sections, accompanied by plots of the observed and best fit lognormal distributions, are presented in Figure 4. The granular nature of the ice is evident in the photograph from a depth of 1 cm. At a depth of 10 cm we see the onset of columnar growth along with the appearance of cellular substructure within the crystals. Near the bottom of the ice (30 cm) the columnar crystals have become well developed and are similar to the young ice example, though due to the slow growth rate, the platelet width was larger. The two large, dark features in the 30-cm photograph are cross sections of vertically oriented brine channels. The brine volume was largest in this section, as was the number density of the brine pockets, though the mean inclusion area was less than the granular ice values. As was true for the young ice case, the CDFs of inclusion size are fit by a lognormal distribution. A notable feature is the presence of both air bubbles and brine pockets in the top section (depth of 1 cm). The air bubbles resulted from the agitated nature of the initial ice growth. Comparing the air bubbles and brine pockets in the top section, we see that there were roughly 3 times as many brine pockets as air bubbles but the air bubbles were larger, with a mean area about 5 times greater (0.28 mm^2 versus 0.046 mm^2). The size distributions for the air bubbles and brine pockets are well separated and easily distinguishable. Since there were only 61 air bubbles in the section, the observed CDF is not as smooth as in the other cases. Comparing results from all four thin sections showed that the frazil ice had the largest mean brine pocket area and also the largest individual pockets.

First-Year Ice

In early May of 1994, near the end of the growth season, we sampled shore-fast first-year ice in the Beaufort Sea at Barrow, Alaska. The physical properties of the ice are summarized in Figure 5. The ice was 1.72 m thick, and though it was warming, it had not undergone any surface melting. Brine volumes were 6–7% in the interior of the ice, increasing to 13% near the bottom. Ice at this location consisted entirely of columnar congelation ice, which included about 10 cm of fine-grained transition ice at the top of the sheet. A significant alignment of c axes had occurred by 30 cm, increasing to very strong alignments in the bottom half of the ice sheet. A slight (10°–15°) swing in the c axis alignment direction, as indicated in the sections from 73 and 162 cm, is attributed to the effects of nearby pressure ridging that occurred during the latter stages of ice growth, leading to a small deflection of the prevailing shoreline current.

Figure 6 shows photomicrographs of six horizontal thin sections taken for analysis from depths of 4 cm, 10 cm, 30 cm, 75

Figure 3. (opposite) (a) Photograph of pancake ice grown in an outdoor pool using a wave maker. The ice was 12 cm thick at the time the photograph was taken. (b) A 30-cm-long vertical thin sections of the pancake ice photographed using polarized light.
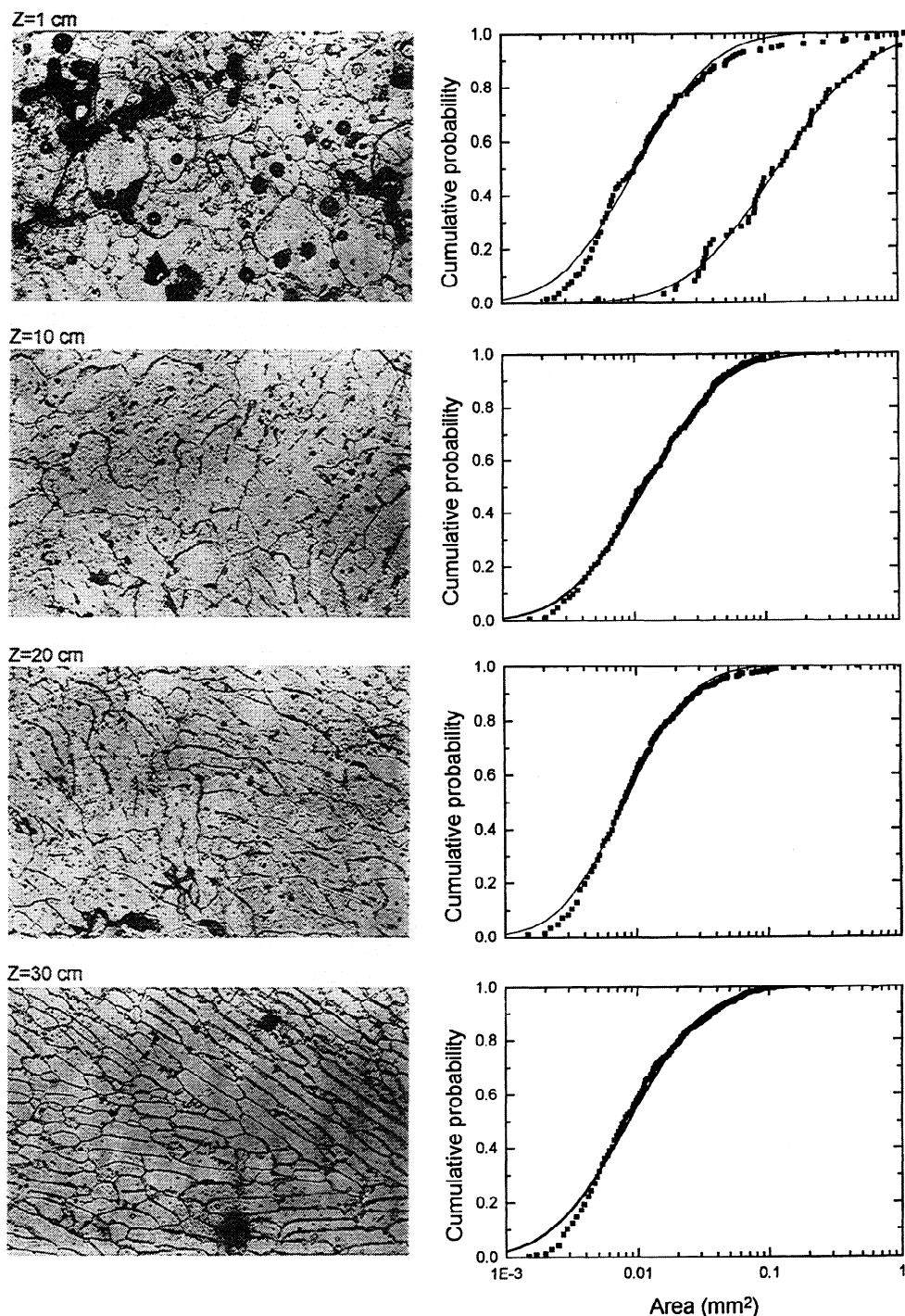
Figure 4. Horizontal thin sections of pancake ice taken at depths of 1, 10, 20, and 30 cm. Plotted are observed (solid squares) and best fit (curve) cumulative brine pocket size distributions. For the top section, results are also presented for air bubbles (rightmost curve).

cm, 119 cm, and 171 cm. Except for the top 10 cm (including the section at 4 cm), which consists of granular transition ice, the remaining sections are all composed of columnar congelation ice exhibiting the diagnostic ice plate/brine pocket substructure of the individual crystals that is the trademark of this particular ice type.

The brine pocket size distributions for these six cases, as well as vertical profiles of brine pocket mean area and number density, are summarized in Figure 7. Both the size distribution

and the summary statistics (Table 1) show significantly larger brine pockets at 4 cm. The 4-cm size distribution is clearly separated from the other cases, and the mean area of 0.056 mm² is almost double that of any of the other five sections. The 10-cm-deep section had the second largest brine pockets, which while smaller than the 4-cm case were significantly larger than those found deeper in the ice. The remaining four sections showed little variability, with mean areas from 0.019 to 0.023 mm² and size distributions that were quite similar. We
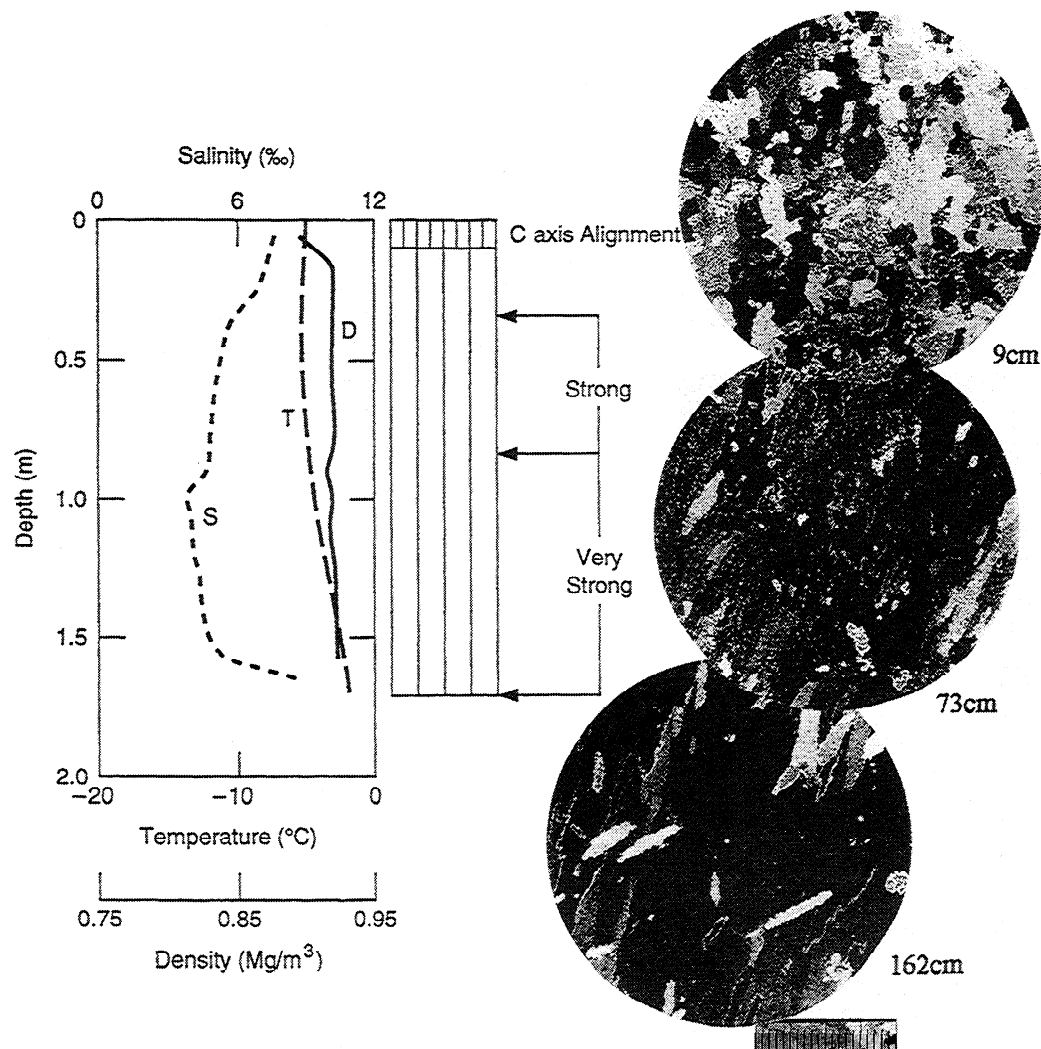
Figure 5. Physical properties of shore-fast, 1.72-m-thick, first-year ice from the Beaufort Sea at Barrow, Alaska. Plotted are ice temperatures (T), salinities (S), and densities (D). Horizontal thin sections from depths of 9 cm, 73 cm, and 162 cm show the columnar structure of the ice and the c axis alignment. The small scale at the bottom of the figure is 2 cm long.

believe that larger brine pockets found in the upper portion of the ice were due to the presence of frazil ice and transition-columnar ice and to partial thermal retexturing of this part of the ice. The bottom four sections, from 30 cm to 171 cm, consisted completely of columnar ice that exhibited no signs of retexturing. Examining the number density of brine pockets shows that the top two sections had the fewest brine pockets, while there was an increase in number density near the bottom where the brine volume was greatest. In the c axis–aligned ice, the elongated brine pockets were also somewhat aligned, with over 35% of the pockets oriented parallel to the long axes of the platelets. Such strong orientation of the brine pockets was not evident in the unaligned ice in the upper part of the ice sheet.

Multiyear Hummock

During the summer melt season, first-year ice undergoes profound changes as it evolves into multiyear ice. First, the snow cover melts; then melting of the ice surface begins. Concurrently, the interior of the ice warms due to the absorption of solar radiation and conduction, causing an increase in brine

volume. There is flushing of the surface melt water and brine drainage in the ice [Untersteiner, 1968; Weeks and Ackley, 1982; Gow and Tucker, 1990], leading to significant desalination. Over time, with dynamic and thermodynamic contributions, the ice surface develops surface relief. There are depressions where melt ponds can form and raised areas called hummocks. The hummocks are well above freeboard, facilitating brine drainage. As drainage occurs, brine pockets are transformed into air bubbles, resulting in bubbly ice with a lower density.

We were able to sample a multiyear hummock not far from the site of the first-year ice observations. The hummock ice was more than 3 m thick. The top 75 cm had completely desalinated resulting in fresh ice with inclusions of air bubbles rather than brine pockets. Figure 8a shows air bubbles in a horizontal thin section taken from a depth of 21 cm in the hummock ice. The dark lines in the photograph are grain boundaries. The air bubbles in the hummock ice were characterized by analyzing 11 thin sections taken from depths of 2 cm, 7 cm, 12 cm, 21 cm, 24 cm, 27 cm, 32 cm, 50 cm, 53 cm, 57 cm, and 64 cm. The number density of air bubbles in the hummock sections was

Z=4 cm

Z=10 cm

Z=30 cm

Z=75

Z=119 cm

Z=171 cm
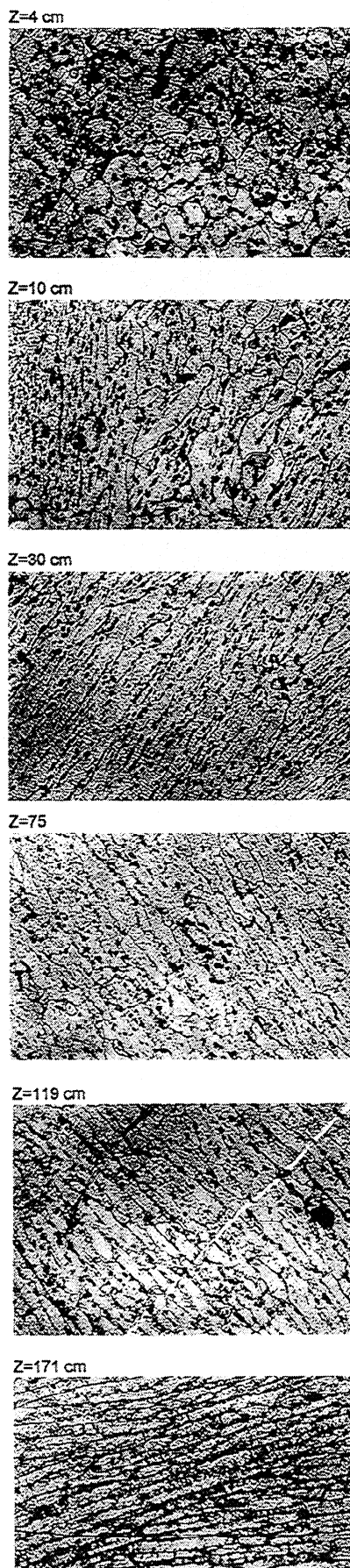
much less than that of brine pockets in the young ice and first-year ice. Because of this, we first combined the measurements from all 11 sections, totaling over 1000 air bubbles, for analysis. The observed and best fit air bubble size distributions for these combined results are plotted in Figure 8b. As was the case for brine pockets, the CDF for the air bubble size was fit by a lognormal distribution (correlation coefficient = 0.996). The mean and median air bubble areas for the top 75 cm of the hummock were 0.64 mm^2 and 0.11 mm^2, respectively, and the number density was 0.23 bubble mm^{-3}. These air bubbles were somewhat smaller than the case studied by *Shokr and Sinha* [1994]. They reported a mean circle-equivalent diameter of 2.36 mm, compared to a value of 0.9 mm for the top 75 cm of this hummock.

A visual inspection of the hummock ice core showed considerable variability, including bands of bubbles. The quantitative analysis of individual thin sections confirmed this, with vertical variations of a factor of 4 in mean area (0.25 mm^2 to 1.15 mm^2) and a factor of 3 in number density (0.14 bubble mm^{-3} to 0.41 bubble mm^{-3}). This vertical variability is examined in the inset in Figure 9, where air bubble number density and mean area are plotted as a function of depth. There is also variability in the air bubble size distributions at different depths, as indicated by the range of values from section to section for the coefficients for the lognormal fit (Table 1). While some of this variability is due to insufficient statistics because of the small number of air bubbles, some of it is real. From the visual inspection it was evident that there were sections that contained big bubbles and sections that had small bubbles. To examine variability with depth of air bubble size but eliminate effects due to insufficient statistics, we selected the five sections with more than 100 bubbles. Plotted in Figure 9 are the best fit CDF for these sections, plus for comparison, the best fit CDF for all 11 sections combined. There are substantial differences between the curves, particularly for smaller bubbles. It is noteworthy that the two extreme curves on the plot are from adjacent sections at depths of 24 cm and 27 cm, illustrating how quickly the air bubble size properties can change.

Effects of Temperature

The previous examples have presented inclusion size distributions for young ice, first-year ice, and a multiyear hummock and have illustrated the changes in the brine and air inclusions that occur as sea ice forms, grows, and eventually melts. Changes in the internal state of the ice also impact the inclusion size distribution. In particular, changes in ice temperature are directly reflected in changes in brine volume, which in turn impact the statistics of the brine pockets. We conducted a laboratory experiment exploring the effects on brine pocket statistics of the increase in brine volume that occurs as the ice warms. A horizontal thin section was prepared from near the bottom of 20-cm-thick lead ice (Beaufort Sea, springtime lead). The ice was columnar with c axes horizontal and had a salinity of 8 ppt. The thin section (Figure 10) was placed on a temperature-controlled stage and warmed in stages from $-20°C$ to $-10°C$ to $-5°C$ to $-2°C$ to $-1°C$. The increase in

Figure 6. (opposite) Horizontal thin sections taken from 1.72-m-thick first-year ice at depths of 4 cm, 10 cm, 30 cm, 75 cm, 119 cm, and 171 cm. The photographs are approximately 2 cm wide.
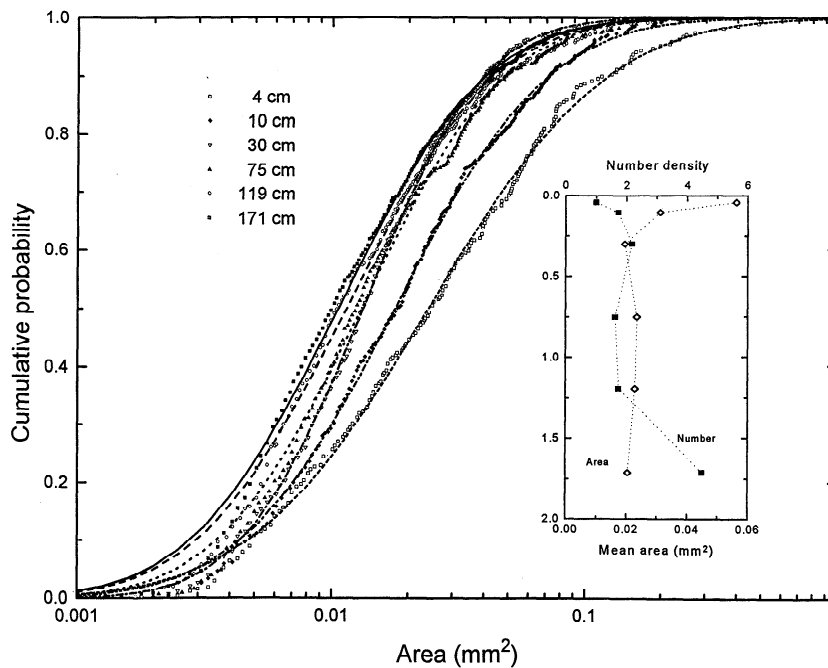
Figure 7. Observed and best fit lognormal cumulative brine pocket size distributions for thin sections from depths of 4 cm, 10 cm, 30 cm, 75 cm, 119 cm, and 171 cm in 1.72-m-thick first-year ice. Plotted in the inset are vertical profiles of brine pocket mean area and number density.

brine volume during this warming and the changes in the brine pocket geometry are displayed in Figure 10.

If we assume, in a simplistic sense, that the brine pockets don't interconnect during warming, then we would expect that as the brine volume increases during warming, (1) the number of brine pockets would remain constant, (2) the mean and median brine pocket area would increase progressively with brine volume, (3) the inclusion size distribution would uniformly shift toward larger sizes, and (4) the "μ" parameter in the lognormal distribution would increase proportionally with brine volume, while the "σ" remained unchanged. If the brine pockets did interconnect, then (1) the number of brine pockets would decrease and (2) the inclusion size distribution and the mean and median would increase even more rapidly with brine volume. Our observational results differ significantly from these scenarios.

The number and the mean area of the brine pockets are plotted as a function of brine volume in Figure 11. At first, from brine volumes of 3% to 8%, the mean area remains essentially constant. As the ice continues to warm, the mean area of the brine pockets increases gradually as the brine volume increases from 8% to 20%, then sharply from 20% to 40%. Part of this sharp increase in size is due to individual brine pockets coalescing to form fewer, larger pockets. The coalescence of brine pocket is also manifested in a decrease in the number density as the brine volume increases from 20% to 40%. Somewhat surprisingly, there was an increase in the number density of brine pockets as the brine volume increased from 3% to 20%. This was perplexing, in that it implied that brine pockets were either fragmenting or being created during warming. Observations confirmed that brine pockets do not fragment during warming; if anything, they coalesce. A closer examination of thin sections during warming showed that brine pockets were not being created. However, brine pockets that

initially were too small to be resolved by our image-processing techniques were increasing in size during warming until they could be detected, thus giving the appearance of brine pockets being created.

The best fit lognormal brine pocket size distributions for the five temperatures are plotted in Figure 12. Results for the $-20°$, $-10°$, and $-5°$C cases are closely intertwined with CDFs that are quite similar and can be distinguished from one another only with difficulty. While the brine volume is doubling between these cases, the absolute changes may be too small for any substantive differences in the size distribution to become evident. There are, however, significant changes in the CDF for the $-2°$C and $-1°$C cases. These distributions are shifted noticeably toward larger inclusions and are distinct from one another and from the lower temperature results. To further generalize the results, we now examine the lognormal parameters μ and σ as a function of ν_b. As the inset in Figure 12 indicates, values are fairly constant, without a clear trend, from brine volumes of 2% to 8%; then both parameters increase with brine volume. This indicates that both the median and the variance of the distribution are increasing.

As the ice warmed, the shape of the inclusions changed as the brine pockets grew more elongated. This is evident in an increase in mean circularity from 24 ($T = -20°$C) to 36 at ($T = -1°$C). This increase is consistent with our qualitative observations. As the ice warms, the brine pockets enlarge along the linear boundaries between ice platelets, giving them an elongated shape. Furthermore, individual brine pockets begin to connect along these linear boundaries, resulting in additional elongation of the brine pockets. This study is somewhat artificial since it is limited to examining the changes that occur in a horizontal section. For ice in situ we would also expect there to be elongation and coalescence of brine pockets in the vertical, eventually resulting in brine drainage.
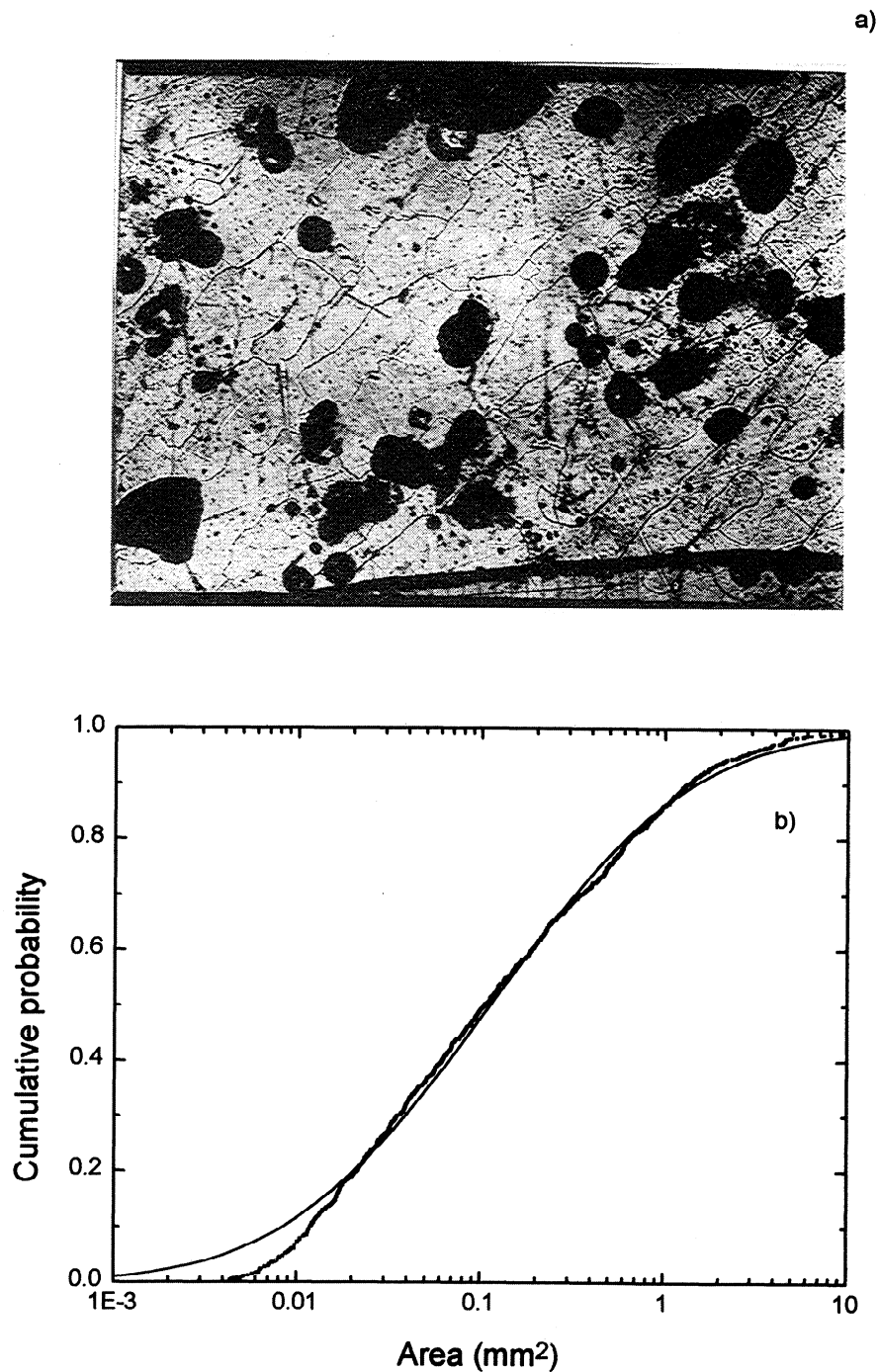
Figure 8. Air bubbles in a multiyear hummock. (a) Horizontal thin section of a multiyear hummock. The small squares in the photograph are 1 mm across. (b) Observed and best fit lognormal cumulative size distribution for air bubbles in a multiyear hummock based on the analysis of 11 thin sections.

Discussion

While a cumulative lognormal distribution does a good job of fitting the inclusion size distributions for a wide range of sea ice types and conditions, the parameters of the fit and other inclusion statistics do change with ice type. In particular, there are significant differences between brine pockets in first-year ice and air bubbles in a multiyear hummock. To illustrate these differences, we shall now directly compare the brine pocket observations from the first-year ice to the air bubble measurements from a multiyear hummock. These two ice types were found near one another and provide an example of the great degree of small-scale variability found in ice properties. The comparison was made using results from the top 0.75 m of each ice type. Eleven thin sections were analyzed for the hummock and four for the first-year ice, giving a total of over 1000 air bubbles and 1400 brine pockets.

Cumulative size distributions for these two cases are plotted in Figure 13 and inclusion statistics are compared in Table 2. Most notable is the clear separation of the distributions for brine pockets and air bubbles. Air bubble areas are much
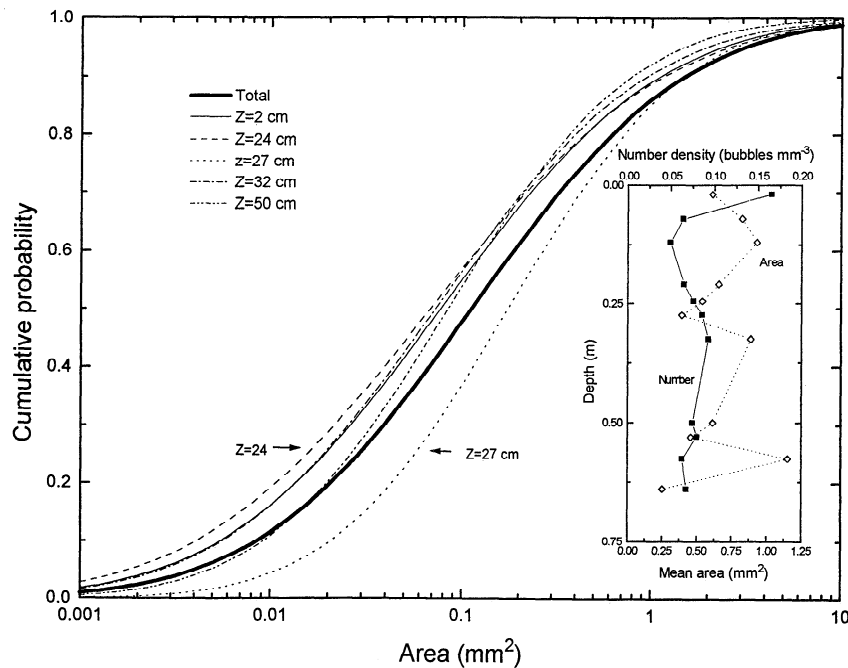
Figure 9. Best fit cumulative air bubble size distributions for a multiyear hummock. Horizontal thin sections from depths of 2 cm, 24 cm, 27 cm, 32 cm, and 50 cm were analyzed. Vertical profiles of air bubble number density and mean area are plotted in the inset.

larger than those of brine pockets. Mean areas of air bubbles are 20 times greater than brine pockets, while median areas of air bubbles are 7 times as large and major axis lengths 3 times bigger (Table 2). The range of sizes for air bubbles is also greater as is evidenced by the divergence of the two size distributions in Figure 13 and the larger value of σ in the air bubble lognormal fit. There are, however, considerably fewer air bubbles than brine pockets, with number densities 4 times larger for brine pockets in the first-year ice than for air bubbles in the multiyear hummock.

The shapes of air bubbles and brine pockets are also different. Air bubbles were less elongated than brine pockets, with median circularities of 19 and 25, respectively. A closer look at the inclusion shape of brine pockets and air bubbles is presented in Figure 14, where the inclusion area is plotted versus

perimeter. The larger size of the air bubbles is evident in Figure 14. The air bubbles tend to fall closer to the area-perimeter line defined by a circle. The brine pockets are more widely spread, with a greater range of perimeters for a given area. This indicates both greater variability in brine pocket shape and greater elongation of the brine pockets.

Though not as pronounced as the differences between air bubbles and brine pockets, there is also variability in the properties of the brine pockets for the young ice, first-year ice, and warming phase cases (Table 1). Possible sources of this variability are differences in the brine volume, ice type (granular or columnar), growth rate, and ice thermal history. For example, there is a weak, general trend toward increases in mean area and circularity with increased brine volume, but there is considerable scatter. This scatter indicates that there may be other influential parameters that need to be considered. Similarly, results indicate that for a comparable brine volume, the mean brine pocket area of granular ice is roughly twice that of columnar ice (Table 1). However, growth rates were also larger for granular ice, leaving the relative importance of ice type and growth rate on brine pocket size unclear. More data are needed to clarify the dependence of brine pocket properties on the ice physical properties and growth parameters.

The work presented in this paper is a step in ascertaining inclusion size distributions for sea ice, but more needs to be done. Experimentally, additional observations are required and other technologies need to be explored. The experimental technique used in this work is limited by the necessity of using thin sections rather than bulk ice samples. However, to address issues such as ascertaining the impact on inclusions of brine drainage during warming and obtaining a true three-dimensional description of the inclusions, analyzing thin sections is not sufficient. In these cases other, "non-destructive" methods of probing the ice interior such as X ray tomography [Kawamura, 1988, 1990] and magnetic resonance imaging

Table 2. Comparison of Air Bubbles in a Multiyear Hummock and Brine Pockets in First-Year Ice

	Multiyear Hummock	First-Year Ice
Statistics		
Number	1040	1792
Total volume, mm³	13,000	1100
Number density, No. mm⁻³	0.08	1.6
Mean area, mm²	0.64	0.029
Median area, mm²	0.11	0.015
Mean axis length, mm	0.84	0.28
Median axis length, mm	0.52	
Mean perimeter, mm	2.59	0.79
Median perimeter, mm	1.49	
Mean circularity	22.2	28.5
Mean circularity	19.1	24.9
Cumulative Lognormal		
Antilog (μ)	0.1126	0.0153
σ	2.014	1.047
R^2	0.996	0.998

T=-19°C

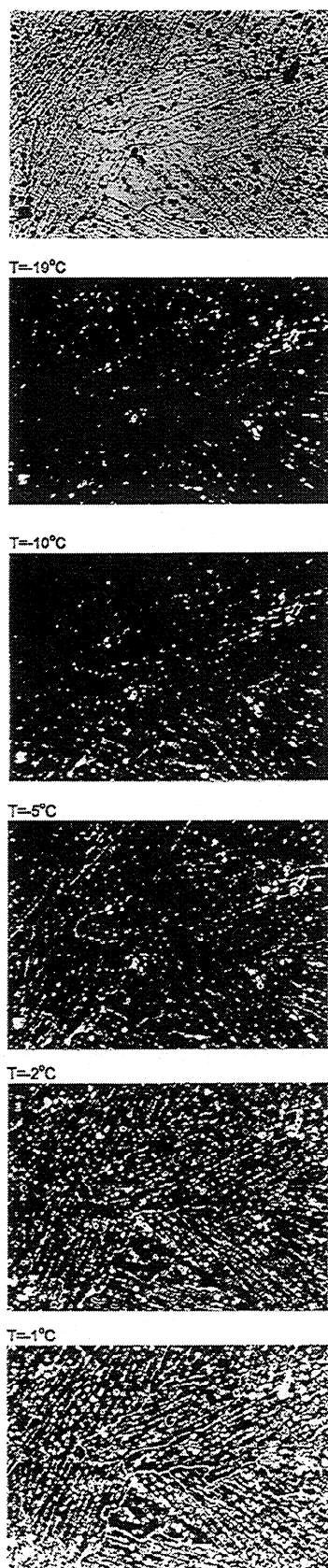T=-10°C

T=-5°C

T=-2°C

T=-1°C

Figure 10. Photograph sequence of the increase in brine volume during warming. The top photograph shows the thin section under natural light. The other photographs are binarized images delineating ice (black) and brine (white) as the section warms from −19°C to −10°C to −5°C to −2°C to −1°C. The photographs are approximately 2 cm wide.
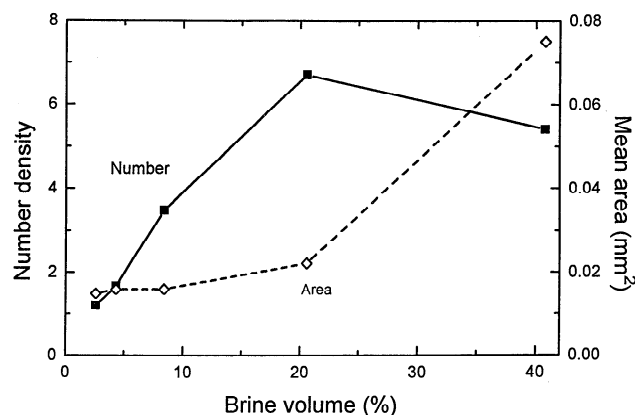

Figure 11. The number density, i.e., number of brine pockets per cubic millimeters (solid squares), and mean area (open diamonds) of brine pockets as a function of brine volume for the warming experiment.

(MRI) [*Edelstein and Schulson*, 1991] are worth investigating. At present, the standard X ray and MRI equipment does not have the requisite spatial resolution for brine pocket characterization, but sufficient resolution may be obtainable with special research quality equipment.

The size distribution of brine pockets in the vertical plane needs to be determined. Brine pockets are elongated with much larger dimensions in the vertical than in the horizontal. Studies of changes in brine pocket size in the vertical dimension during warming are of particular interest, since they would help determine the porosity at which the brine pockets interconnect, greatly enhancing brine drainage. An accurate representation of the vertical structure of brine pockets could be obtained from vertical thin sections taken from oriented and aligned ice. These sections could be placed vertically and warmed, allowing a two-dimensional investigation of the effects of vertical brine drainage.

With the currently available technology it is now fairly straightforward to analyze sea ice thin sections and calculate a host of statistical measures defining the ice microstructure. This ease of calculation accentuates the importance of knowing a priori what description is needed for a particular application. It is far too easy to be buried in a morass of detailed but irrelevant statistics. In a similar vein, knowing the appropriate scale of investigation is also important. The microstructure analysis of air bubbles and brine pockets presented in this paper is appropriate for many optical and microwave studies. In other cases an analysis on a larger scale examining parameters such as the grain size or the distribution of brine channels might be appropriate [*Wakatsuchi and Saito*, 1985; *Wakatsuchi and Kawamura*, 1987].

In some instances, perhaps an even smaller-scale examination might be required. Figure 15 shows the ice microstructure of frazil ice magnified by an additional factor of 10 compared to the 1-cm-deep pancake ice section shown in Figure 4a. The large central feature is an air bubble, and the smaller elongated features are brine pockets. The photograph provides a visual confirmation of our basic conclusions that the air bubbles are rounder and much bigger than the brine pockets. But what is truly interesting about the photograph is that a closer examination shows that many of the brine pockets contain very small air bubbles, providing an additional level of complexity. We suspect that these small air bubbles occur during warming of
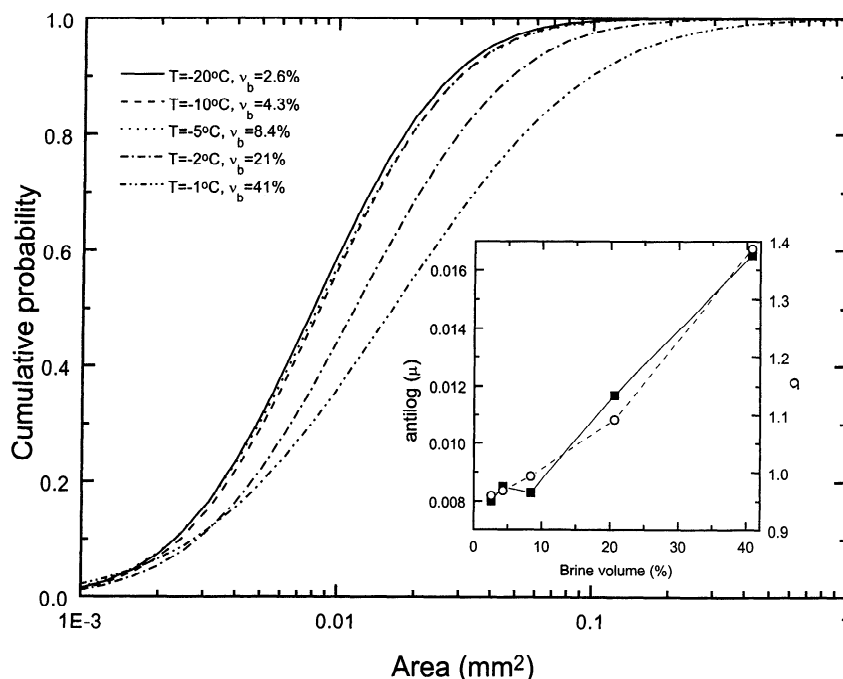
Figure 12. Best fit lognormal brine pocket size distributions during the warming experiment. Results are for ice temperatures of −20°C, −10°C, −5°C, −2°C, and −1°C. The coefficients of the lognormal fit are plotted as a function of brine volume in the inset.

the ice. As the ice warms, the ice-brine mixture stays in equilibrium by increasing the brine volume through the melting of ice adjacent to the brine pocket [*Weeks and Ackley*, 1982]. There is a 10% volume reduction associated with this ice to brine phase change that may result in the formation of small air bubbles in the brine pocket. Thus these small air bubbles are roughly one-tenth the volume of the brine pockets in which they are contained. Extending the analysis to a smaller scale would also test the applicability of the lognormal distribution over a wider range of inclusion sizes.

Our understanding of inclusion size distributions needs to be further generalized. The characteristics of the inclusions can be summarized by three parameters: the number density, μ, and σ. Relationships between these three parameters and the physical properties of the ice need to be determined. We have begun to explore the effects of ice temperature and ice type. This exploration must be continued, and other factors, such as growth conditions and salinity, also need to be investigated.
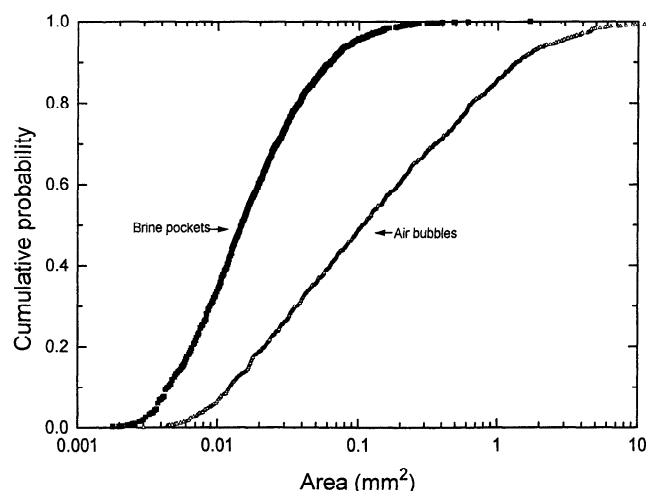

Figure 13. Comparison of size distributions for brine pockets and air bubbles. Observed distributions for brine pockets in first-year ice (solid squares) and air bubbles in a multiyear hummock (open triangles) are presented.
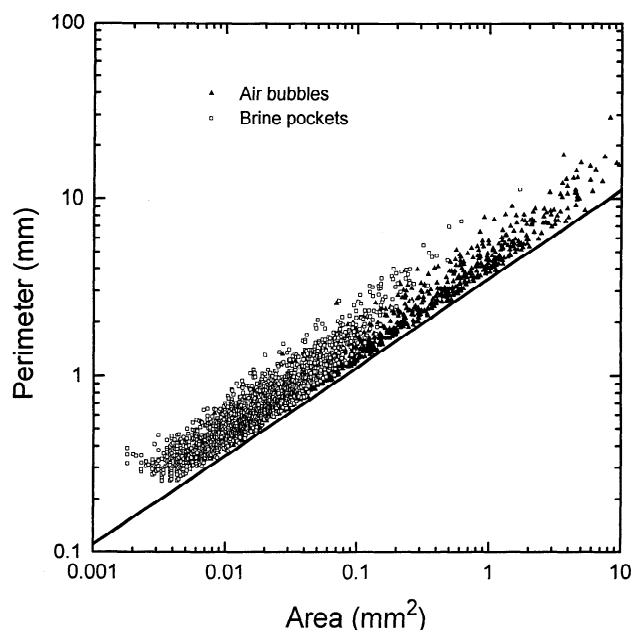

Figure 14. Plot of inclusion area versus perimeter for air bubbles in a multiyear hummock and brine pockets in first-year ice. Observations of more than 1000 air bubbles and 1400 brine pockets are plotted. The solid line denotes the smallest possible area-to-perimeter relationship, that of a circle.

Figure 15. Pancake ice thin section at 10 times the magnification of Figure 4. The large central feature is an air bubble and the smaller elongated features are brine pockets. Note that some of the brine pockets contain even smaller air bubbles (C).

Parameterizations of the lognormal coefficients μ, σ as a function of growth rate, growth conditions, salinity, and brine volume could be generated. There are existing models of sea ice physical properties that, given environmental forcing parameters, can compute vertical profiles of ice temperature, salinity and brine volume [*Cox and Weeks*, 1988]. Information on inclusion size distribution and statistics could be incorporated into these physical properties models, giving a model that would not only determine the amount of brine but would also estimate the size distribution of the brine pockets. Such a goal for young ice and first-year ice is attainable.

The real difficulty lies in the transitioning of first-year ice to multiyear ice during the summer. As first-year ice undergoes a melt season, the collection of many small, elongated brine pockets evolves into a group of fewer larger, rounder air bubbles. Understanding the details of this evolution is a key issue in ice physical properties work. On the basis of the warming experiment we can speculate that during the melt season, the brine pockets grow larger as the brine volume increases and individual pockets coalesce. For ice above the freeboard, as the large brine pockets become larger and connect, eventually they will drain, leaving air voids behind. An unresolved issue is how these very elongated brine pockets develop into the rounder air bubbles. The evolution of first-year ice into multiyear ice is an area that needs more study both qualitatively and quantitatively.

Conclusions

The cross-sectional areas of sea ice inclusions, over the size range studied, are fit by a two-parameter cumulative lognormal distribution. This is true for both brine pockets and air bubbles

and for a range of ice types and conditions. The values of the parameters vary, but the functional dependence of the size distribution does not. The two parameters of the distribution are the mean (μ) and standard deviation (σ) of the natural logarithm of the area. These parameters can be directly computed from observations of inclusion cross-sectional area, thereby generating the cumulative lognormal size distribution of the inclusions.

Air bubbles in a multiyear hummock are much larger than brine pockets in young ice and first-year ice, with mean major axis lengths of the order of millimeters for air bubbles and tenths of a millimeter for brine pockets. The shape of the brine pockets is more elongated than that of the air bubbles. As ice warms, and its brine volume increases, the size distribution shifts toward larger brine pockets. This increase in brine pocket size is particularly pronounced for brine volumes greater than 10% as individual brine pockets coalesce.

References

Arcone, S. A., A. J. Gow, and S. McGrew, Structure and dielectric properties at 4.8 and 9.5 GHz of saline ice, *J. Geophys. Res.*, *91*, 14,281–14,303, 1986.
Armstrong, T., B. Roberts, and C. Swithinbank, *Illustrated Glossary of Snow and Ice*, Scott Polar Res. Inst., Cambridge, England, 1973.

Campbell, J. W., The lognormal distribution as a model for bio-optical variability in the sea, *J. Geophys. Res.*, *100*, 13,237–13,254, 1995.

Colbeck, S. C., Theory of particle coarsening with a log-normal distribution, *Acta Metall.*, *35*, 1583–1588, 1987.

Cox, G. F. N., and W. F. Weeks, Numerical simulations of the profile properties of undeformed first-year sea ice during the growth season, *J. Geophys. Res.*, *93*, 12,449–12,461, 1988.

Davis, N. R., and P. Wadhams, A statistical analysis of Arctic pressure ridge morphology, *J. Geophys. Res.*, *100*, 10,915–10,926, 1995.

Edelstein, W. A., and E. M. Schulson, NMR imaging of salt water ice, *J. Glaciol.*, *37*, 177–180, 1991.

Eicken, H., Automated image analysis of ice thin sections—Instrumentation, methods and extraction of stereological and textural parameters, *J. Glaciol.*, *39*, 341–352, 1993.

Eicken, H., and M. A. Lange, Development and properties of the sea ice in the coastal regime of the southeastern Weddell Sea, *J. Geophys. Res.*, *94*, 8193–8206, 1989.

Eppler, D. T., et al., Passive microwave signatures of sea ice, in *Microwave Remote Sensing of Sea Ice, Geophys. Monogr. Ser.*, vol. 68, edited by F. Carsey, chap. 4, pp. 47–72, AGU, Washington, D. C., 1992.

Frankenstein, G. E., and R. Garner, Equations for determining the brine volume of sea ice from $-0.5°C$ to $-22.9°C$, *J. Glaciol.*, *6*, 943–944, 1967.

Gow, A. J., and W. B. Tucker III, Sea ice in the polar regions, in *Polar Oceanography Part A Physical Science*, edited by W. O. Smith, pp. 122–147, Academic, San Diego, Calif., 1990.

Gow, A. J., S. F. Ackley, K. R. Buck, and K. M. Golden, Physical and structural characteristics of Weddell Sea pack ice, *CRREL Rep. 87-14*, U.S. Army Cold Reg. Res. Eng. Lab., Hanover, N. H., 1987.

Grenfell, T. C., A theoretical model of the optical properties of sea ice in the visible and near infrared, *J. Geophys. Res.*, *88*, 9723–9735, 1983.

Grenfell, T. C., Radiative transfer model for sea ice with vertical structure variations, *J. Geophys. Res.*, *96*, 16,991–17,001, 1991.

Grenfell, T. C., and G. A. Maykut, The optical properties of ice and snow in the Arctic Basin, *J. Glaciol.*, *18*, 445–463, 1977.

Grenfell, T. C., and D. K. Perovich, Spectral albedos of sea ice and incident solar irradiance in the southern Beaufort Sea, *J. Geophys. Res.*, *89*, 3573–3580, 1984.

Grenfell, T. C., D. J. Cavalieri, J. C. Comiso, M. R. Drinkwater, R. G. Onstott, I. Rubenstein, K. Steffen, and D. P. Winebrenner, Considerations for microwave remote sensing of thin sea ice, in *Microwave Remote Sensing of Sea Ice, Geophys. Monogr. Ser.*, vol. 68, edited by F. Carsey, chap. 14, pp. 291–302, Washington, D. C., 1992.

Jandel Scientific, *Table Curve User's Manual*, San Raphael, Calif., 1994.

Jeffries, M. O., K. Schwartz, K. Morris, A. D. Veazey, H. R. Krouse, and S. Cushing, Evidence for platelet ice accretion in Arctic sea ice development, *J. Geophys. Res.*, *100*, 10,905–10,914, 1995.

Johnston, M., and N. K. Sinha, A method for determining the macrostructural statistics of the scattering layer of first-year sea ice from Frederick Hyde Fjord, Greenland, *Proc. Int. Conf. Offshore Mech. Arctic Eng.*, *14*, 203–210, 1995.

Kawamura, T., Observations of the internal structure of sea ice by X ray computed tomography, *J. Geophys. Res.*, *93*, 2343–2350, 1988.

Kawamura, T., Nondestructive, three-dimensional density measurements of ice core samples by X ray computed tomography, *J. Geophys. Res.*, *95*, 12,407–12,412, 1990.

Lange, M. A., S. F. Ackley, P. Wadhams, G. S. Dieckmann, and H. Eicken, Development of sea ice in the Weddell Sea, Antarctica, *Ann. Glaciol.*, *12*, 92–96, 1988.

LEADEX Group, The LEADEX Experiment, *Eos Trans. AGU*, *74*, 393, 396–397, 1993.

Lin, F. C., J. A. Kong, R. T. Shin, A. J. Gow, and S. A. Arcone, Correlation function study for sea ice, *J. Geophys. Res.*, *93*, 14,055–14,063, 1988.

Nakawo, M., and N. K. Sinha, A note on the brine layer spacing of first-year ice, *Atmos. Ocean*, *22*(2), 193–206, 1984.

Onstott, R. G., SAR and scatterometer signatures of sea ice, in *Microwave Remote Sensing of Sea Ice, Geophys. Monogr. Ser.*, vol. 68, edited by F. Carsey, chap. 5, pp. 73–104, AGU, Washington, D. C., 1992.

Optimas, *Optimas 5, User Guide and Technical Reference*, Seattle, Wash., 1995.

Papoulis, A., *Probability, Random Variables and Stochastic Processes*, McGraw-Hill, New York, 1965.

Perovich, D. K., Theoretical estimates of light reflection and transmission by spatially complex and temporally varying sea ice covers, *J. Geophys. Res.*, *95*, 9557–9567, 1990.

Perovich, D. K., Light reflection from sea ice during the onset of melt, *J. Geophys. Res.*, *99*, 3351–3359, 1994.

Perovich, D. K., *The Optical Properties of Sea Ice, CRREL Monogr. 96-1*, 25 pp., U.S. Army Cold Reg. Res. and Eng. Lab., Hanover, N. H., 1996.

Perovich, D. K., and A. J. Gow, A statistical description of the microstructure of young sea ice, *J. Geophys. Res.*, *96*, 16,943–19,953, 1991.

Perovich, D. K., and A. J. Gow, Towards a quantitative characterization of sea ice microstructure, in *IGARRS '92*, vol. 2, pp. 1249–1252, Inst. of Electr. Eng., Piscataway, N. J., 1992.

Perovich, D. K., and T. C. Grenfell, Laboratory studies of the optical properties of young sea ice, *J. Glaciol.*, *27*, 331–346, 1981.

Perovich, D. K., and A. Hirai, Microcomputer based image processing system, *J. Glaciol.*, *34*, 249–252, 1988.

Richter-Menge, J. A., and D. K. Perovich, An overview of sea ice optical properties and their variability, in *Ocean Optics 11, Proc. SPIE Int. Soc. Opt. Eng.*, *1750*, 486–497, 1992.

Sachs, L., *Applied Statistics: A Handbook of Techniques*, Springer-Verlag, New York, 1978.

Shokr, M. E., and N. K. Sinha, Arctic sea ice microstructure observations relevant to microwave scattering, *Arctic*, *47*(3), 265–279, 1994.

Stogryn, A., Correlation functions for random granular media in strong fluctuation theory, *IEEE Trans. Geosci. Remote Sens.*, *GE 22*, 150–154, 1984.

Tsang, L., and J. A. Kong, Scattering of electromagnetic waves from random media with strong permittivity fluctuations, *Radio Sci.*, *16*, 303–320, 1981.

Tucker, W. B., III, A. J. Gow, and W. F. Weeks, Physical properties of summer sea ice in the Fram Strait, *J. Geophys. Res.*, *92*, 6787–6803, 1987.

Tucker, W. B., III, T. C. Grenfell, R. G. Onstott, D. K. Perovich, A. J. Gow, and R. A. Shuchman, Microwave and physical properties of sea ice in the winter marginal ice zone, *J. Geophys. Res.*, *96*, 4573–4589, 1991.

Tucker, W. B., III, D. K. Perovich, A. J. Gow, W. F. Weeks, and M. R. Drinkwater, Physical properties of sea ice relevant to remote sensing, in *Microwave Remote Sensing of Sea Ice, Geophys. Monogr. Ser.*, vol. 68, edited by F. Carsey, chap. 2, pp. 9–28, AGU, Washington, D. C., 1992.

Untersteiner, N., Natural desalination and equilibrium salinity profile of old sea ice, *J. Geophys. Res.*, *73*, 1251–1257, 1968.

Vallese, F., and J. A. Kong, Correlation function studies for snow and ice, *J. Appl. Phys.*, *52*, 4921–4925, 1981.

Wakatsuchi, M., and T. Kawamura, Formation processes of brine drainage channels in sea ice, *J. Geophys. Res.*, *92*, 7195–7197, 1987.

Wakatsuchi, M., and T. Saito, On brine channels in young sea ice, *Ann. Glaciol.*, *6*, 200–202, 1985.

Weeks, W. F., and S. F. Ackley, *The Growth, Structure, and Properties of Sea Ice, CRREL Monogr. 82-1*, 130 pp., Cold Reg. Res. and Eng. Lab., Hanover, N. H., 1982.

Weeks, W. F., and A. J. Gow, Preferred crystal orientations in the fast ice along the margins of the Arctic Ocean, *J. Geophys. Res.*, *83*, 5105–5121, 1978.

Weeks, W. F., and A. J. Gow, Crystal alignments in the fast ice of Arctic Alaska, *J. Geophys. Res.*, *85*, 1137–1146, 1980.

Winebrenner, D. P., L. Tsang, B. Wen, and R. West, Sea ice characterization measurements needed for testing of microwave remote sensing models, *IEEE J. Oceanic Eng.*, *14*, 149–158, 1989.

Winebrenner, D. P., et al., Microwave sea ice signature modeling, in *Microwave Remote Sensing of Sea Ice, Geophys. Monogr. Ser.*, vol. 68, edited by F. Carsey, pp. 137–176, AGU, Washington, D. C., 1992.

A. J. Gow and D. K. Perovich, U.S. Army Cold Regions Research and Engineering Laboratory, 72 Lyme Road, Hanover, NH 03755. (e-mail: perovich@hanover-crrel.army.mil)